

Detection of CO $J = 1 - 0$ in the $z = 3.79$ Radio Galaxy 4C 60.07

T.R. Greve¹, R.J. Ivison², and P.P. Papadopoulos^{3,4},

¹ Institute for Astronomy, University of Edinburgh, Blackford Hill, Edinburgh EH9 3HJ, United Kingdom
e-mail: tgreve@roe.ac.uk

² UK ATC, Royal Observatory, Blackford Hill, Edinburgh EH9 3HJ, United Kingdom
e-mail: rji@roe.ac.uk

³ Department of Physics & Astronomy, University College London, Gower Street, London WC1E 6BT, United Kingdom
e-mail: pp@star.ucl.ac.uk

⁴ Sterrewacht Leiden, P. O. Box 9513, 2300 RA Leiden, The Netherlands

Received December 2, 2003; accepted February 5, 2004

Abstract. We report on the detection of the lowest CO $J = 1 - 0$ transition in the powerful high-redshift radio galaxy 4C 60.07 at $z = 3.79$. The CO emission is distributed in two spatially and kinematically distinct components as was previously known from the observations of the higher excitation CO $J = 4 - 3$ line. The total molecular gas mass in 4C 60.07 inferred from the CO $J = 1 - 0$ emission is $M(\text{H}_2) \simeq 1.3 \times 10^{11} M_\odot$, sufficient to fuel the inferred star-formation rate of $\sim 1600 M_\odot \text{ yr}^{-1}$ for 10^8 yrs. From our high-resolution CO $J = 1 - 0$ VLA maps we find the dynamical mass of 4C 60.07 to be comparable to that of a giant elliptical at the present time. A significant fraction of the mass is in the form of molecular gas suggesting that 4C 60.07 is in an early state of its evolution. The merging nature of 4C 60.07 along with its large dynamical mass imply that this system is a giant elliptical caught in its formative stages.

Key words. Galaxies: individual: 4C 60.07 – galaxies: active – galaxies: formation – galaxies: ISM – cosmology: observations

1. Introduction

High-redshift radio galaxies (HzRGs) are amongst the most luminous objects known, and are believed to serve as tracers of the peaks of the primordial density field around which giant elliptical galaxies and clusters of galaxies form (Kauffmann 1996; West et al. 1994). In the radio, HzRGs typically display a double-lobe morphology and large radio luminosities ($P_{178 \text{ MHz}} \sim 5 \times 10^{35} \text{ erg s}^{-1} \text{ Hz}^{-1}$), indicating a highly active black hole.

Recently, evidence has been mounting that HzRGs are massive starburst galaxies. This has come about from sub-millimetre detections of a number of HzRGs, implying large rest-frame far-IR luminosities ($L_{\text{FIR}} \simeq 10^{13} L_\odot$) powered by intense star formation ($SFR \simeq 1000 - 2000 M_\odot \text{ yr}^{-1}$ - Dunlop et al. 1994; Hughes et al. 1997; Ivison et al. 1998; Archibald et al. 2001). In a recent SCUBA survey of seven HzRGs and their surroundings, Stevens et al. (2003) not only found the star formation in the radio galaxies themselves to be extended on several tens of kilo-parsec scales but also found one or

more previously undetected submm sources in the vicinity (50 – 250 kpc) of more than half of the targeted objects. It is difficult to see how the Active Galactic Nucleus (AGN) could power the far-IR luminosity on $\gtrsim 10$ kpc scales, and a massive starburst seems to be the natural explanation. Indeed, adequate "fuel" for such large star formation rates has been found in the four HzRGs which have been detected in CO to date (Papadopoulos et al. 2000; De Breuck et al. 2003a; De Breuck et al. 2003b). These observations revealed the presence of massive ($\sim 10^{11} M_\odot$) reservoirs of molecular gas, enough to fuel a $\sim 1000 M_\odot \text{ yr}^{-1}$ starburst for $\sim 10^8$ yr, and in in half of the cases the CO emission was found to be extended on tens of kpc scales (Papadopoulos et al. 2000; De Breuck et al. 2003a). Similar large molecular gas masses distributed in clumps on tens of kilo-parsec scales has been found in a number of QSOs at high redshifts (Carilli et al. 2002a; Carilli et al. 2002b). In general, HzRGs have the advantage over quasars that they are not gravitationally lensed since they are usually selected on the basis of extended lobe-emission whereas quasars are often found to be lensed. Furthermore, HzRGs are known to be associated with gi-

ant ellipticals in the local Universe (McLure & Dunlop 2000).

In this paper we present high-resolution observations of the CO $J = 1 - 0$ emission from 4C 60.07 at $z = 3.788$ using the Very Large Array¹. Throughout we have assumed $H_0 = 65 \text{ km s}^{-1} \text{ Mpc}^{-1}$, $\Omega_M = 0.3$ and $\Omega_\Lambda = 0.7$. In this cosmology the luminosity distance of 4C 60.07 is 36.2 Gpc and $1''$ corresponds to 7.7 kpc.

2. 4C 60.07

4C 60.07 is an ultra-steep-spectrum (USS) radio galaxy at redshift of $z = 3.788$ (Chambers et al. 1996; Röttgering et al. 1997). It displays a Fanaroff-Riley II (FR II) edge-brightened double-radio morphology (Fanaroff & Riley 1974). The radio morphology of 4C 60.07 is seen in Figure 1 which shows a VLA C-band (6 cm) archive image of 4C 60.07. The system consists of two main bright hot spots separated by about $9''$. The south-eastern component is further comprised of two components (B and C). Continuum emission is also seen from the radio core which is located $\sim 2''$ west-northwest of the C-component.

The CO $J = 4 - 3$ line and 1.25 mm continuum emission from 4C 60.07 have been imaged using the IRAM Plateau de Bure Interferometer (Papadopoulos et al. 2000). The CO emission was found to emerge from two kinematically distinct components separated in velocity space by $\sim 700 \text{ km s}^{-1}$. The component with the narrowest line profile ($FWHM \sim 150 \text{ km s}^{-1}$) is offset by $V \simeq -224 \text{ km s}^{-1}$ from the systemic velocity corresponding to $z = 3.788$ and spatially coincident with the position of the radio core. The broader component ($FWHM \geq 550 \text{ km s}^{-1}$) peaks $\sim 7''$ ($\sim 30 \text{ kpc}$) west of the radio core, and is offset by $\simeq 483 \text{ km s}^{-1}$ from the systemic velocity. Such large offsets between the redshift of the optical emission lines and the CO emission has been observed in several other high redshift systems, and is commonly attributed to the optical lines originating in strong outflows and winds (Guilloteau et al. 1999; Cox et al. 2002). Strong gravitational lensing can be ruled out as the origin of the double source and large apparent luminosity since not only do the two components have different line widths but they are also offset in velocity with respect to each other. Furthermore, there are no indications from observations in the optical and radio suggesting that 4C 60.07 might be lensed.

In order to get a handle on the non-thermal contribution to the submm and CO fluxes, we used C and X band images from the VLA Archive to measure the radio fluxes of the various components in 4C 60.07 at 6 cm and 3.6 cm. In Figure 2 we have plotted the submm/far-IR spectral energy distribution (SED) of 4C 60.07 along with the radio spectra of the A-component and the radio

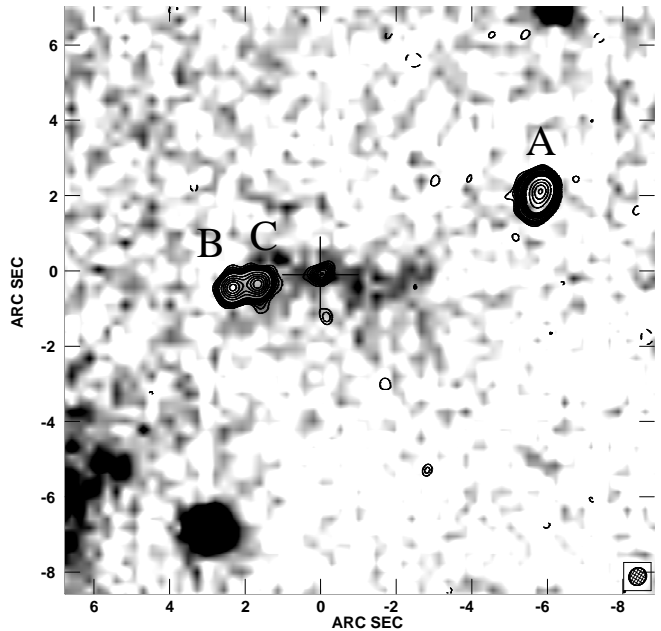


Fig. 1. 6 cm VLA map of 4C 60.07 overlaid on an I-band image obtained with the William Herschel Telescope. The radio hot spots are denoted by A, B and C. The cross marks the position of the radio core: R.A.(J2000): $05^{\text{h}}12^{\text{m}}55^{\text{s}}.147$, DEC.(J2000): $+60^{\circ}30'51''.0$. The insert in the bottom right corner shows the synthesized beam.

core. The A-component (the dotted line in Figure 2) is the brightest component in the radio and furthermore has the shallowest spectral slope ($\alpha_{6 \text{ cm}}^{3.6 \text{ cm}} = -1.4$) which means it provides a strict upper limit on the non-thermal flux at submm wavelengths. The 1.25 mm continuum emission from 4C 60.07 is likely to be thermal in origin, i.e. from warm dust, since non-thermal processes are unable to account for the observed flux, see Figure 2. Furthermore, the 1.25 mm continuum emission is offset by $\sim 4''$ to the west from the radio core position, and does not appear to be associated with the non-thermal emission.

The radio core has a spectral slope of $\alpha_{6 \text{ cm}}^{3.6 \text{ cm}} = -1.7$. Extrapolating to the frequency of the CO $J = 1 - 0$ line ($\sim 24 \text{ GHz}$) we find that the radio continuum is expected to contribute a non-negligible $S_{24 \text{ GHz}} = 0.03 \text{ mJy}$. In comparison, the contribution from the thermal dust spectrum seems completely negligible, see Figure 2.

3. Observations

The CO $J = 1 - 0$ line ($\nu_{\text{rest}} = 115.27 \text{ GHz}$) from 4C 60.07 is redshifted into the VLA's K-band (1.3-cm) receivers. Since non-thermal continuum emission from the radio core was expected, we used two IF pairs (right- and left-hand circular polarisation) centred on the two kinematically distinct emission-line components, each pair set up such that one IF pair was centred on the line and the other pair was offset from this by 100 MHz to measure the continuum. The IF set-up for both the broad and narrow com-

¹ The Very Large Array (VLA) is operated by the National Radio Observatory, which is a facility of the National Science Foundation, operated under cooperative agreement by Associated Universities, Inc.

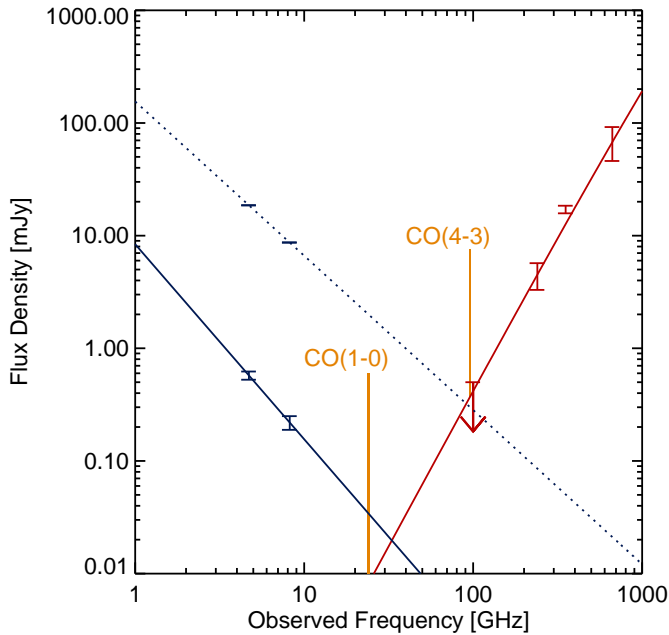


Fig. 2. The submm/far-IR spectral energy distribution (SED) of 4C 60.07 (red line) along with the radio spectra of the A-component (blue dotted line) and the radio core (blue solid line). The submm points are taken from SCUBA observations by Archibald et al. (2001) while the IRAM 30m Telescope data-points at 252 GHz (1.25 mm) and 100 GHz (3 mm) are from Papadopoulos et al. (2000). The radio points are measured from C and X band data of 4C 60.07 from the VLA Archive. The positions and strengths of the CO $J = 1 - 0$ and $J = 4 - 3$ lines relative to the SED are shown in yellow (based on this paper and Papadopoulos et al. (2000)).

ponent is detailed in Figure 3. The broad-line component was observed in continuum mode with a 50 MHz-wide IF centred at 24.035 GHz, which corresponds to a velocity coverage of 624 km s^{-1} . Not only does this not properly cover the broad component but, since the observations were done in continuum mode, no information on the line shape was available, and one therefore has to rely on the IRAM CO $J = 4 - 3$ observations to infer a line width for the broad component. The narrow component was observed in spectral-line mode with a 7-channel IF centred at 24.095 GHz, each channel being 3.125 MHz wide. This was to avoid under-resolving the narrow line in velocity space. However, the line datasets from the 2002 December 20 and 2003 March 09 are centred at 24.089 GHz, corresponding to a shift of two channels, in order to get a better spectral coverage at the low-frequency side of the line. Thus nine channels (denoted channels 1,...,9 in Figure 3) covered the line, corresponding to a velocity coverage of 350 km s^{-1} . 4C 60.07 was observed in the VLA’s CD, D and C configurations (see Table 1). The D-configuration data, however, turned out not to have the spatial resolution required to properly separate the (B,C) component

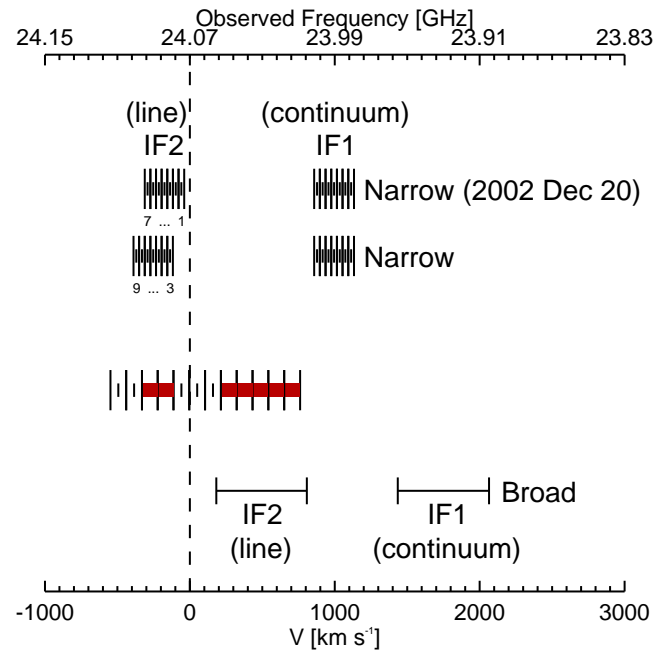


Fig. 3. Velocity and frequency coverage of the IF set-up used in our VLA CO $J = 1 - 0$ observations. The dashed line outlines the systemic velocity corresponding to $z = 3.788$. In red is shown the velocity-channels of the IRAM PdBI observations of Papadopoulos et al. (2000); channels in which CO $J = 4 - 3$ emission was detected are marked in thick red.

from the radio core, and was therefore discarded. The lack of D-array data is very unlikely to result in “filtering out” any extended CO emission since such emission would have to be extended over scales $\gtrsim 60''$ ($\gtrsim 460 \text{ kpc}$). The fact that we do not find any change in total flux after including the D-array data verifies this point.

In total, after calibration overheads, we obtained 6.3 hr of integration time on source for both the broad and narrow components. Calibration and data reduction was done using standard recipes in the NRAO *AIPS* Cookbook. The amplitude was calibrated with the quasars 3C 48 and 3C 286 at the beginning and/or end of each transit. The phase drift was calibrated using a fast-switching technique in which we observed the nearby source 04494+63322 every few minutes. The data were obtained in good weather conditions, and the rms phase fluctuations after calibration was less than 10° . For the spectral-line mode observations of the narrow component, the bandpass of the system was calibrated using 0319+415. In all cases the bandpass calibration averaged over the 7 channels was better than 92%. Data taken at different times and in different configurations were combined using DBCON, weighting each dataset with the its total gridded weight.

4. Results & Analysis

The radio morphology of 4C 60.7 in the broad and narrow component IF set-ups is shown in Figure 4. Figure 4a and

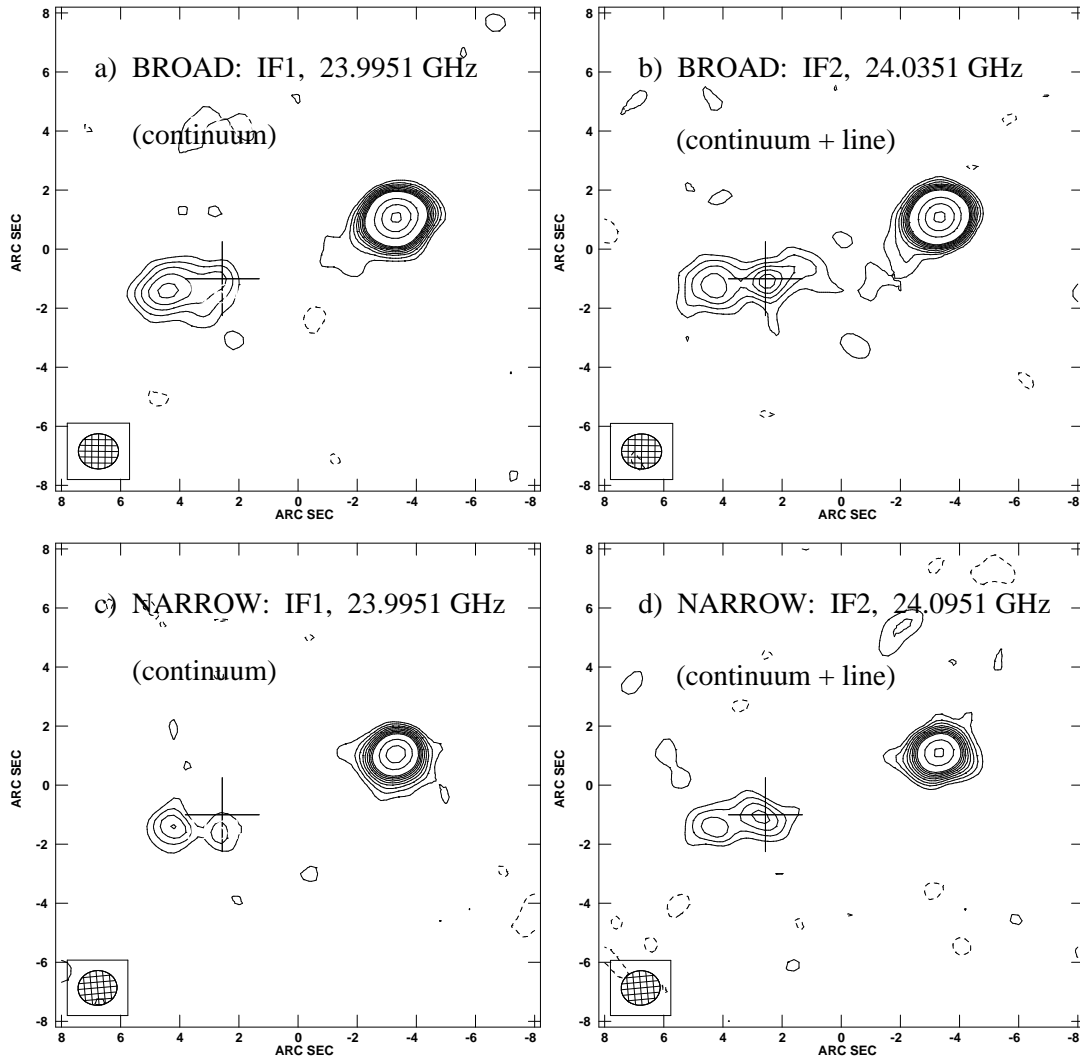


Fig. 4. Naturally weighted, untapered maps, showing the morphology of 4C 60.07 in the two IF set-ups. **Top row:** The spatial resolution is $1''.36 \times 1''.19$ with the major axis P.A. = 89° . The rms noise is $0.030 \text{ mJy beam}^{-1}$. Contours are shown at $-2, 2, 3, 4, 5, 6, 7, 8, 9, 10, 20, 30,$ and $40 \times 35 \mu\text{Jy beam}^{-1}$. **Bottom row:** The spatial resolution (FWHM) is $1''.32 \times 1''.17$ with the major axis P.A. = 275° , and the rms noise level is $0.051 \text{ mJy beam}^{-1}$. Contours are shown at $-2, 2, 3, 4, 5, 6, 7, 8, 9, 10, 15,$ and $20 \times 60 \mu\text{Jy beam}^{-1}$. The cross marks the position of the radio core (R.A.(J2000): $05:12:55.147$, DEC.(J2000): $+60:30:51.0$).

Table 1. VLA Observations.

Date	Configuration	$t_{\text{int}}/\text{hrs}$
2001 Oct 2	CD	1.4
2001 Oct 9	CD	1.7
2001 Oct 11	D	1.7
2001 Oct 19	D	2.8
2002 Nov 12	C	1.7
2002 Dec 20	C	1.5

b show pure continuum emission and continuum emission plus the broad CO line emission, respectively; similarly for Figure 4c and d but for the narrow component.

In Figure 4a, which shows the continuum emission at 23.935 GHz, we recognise the two radio lobes seen in Figure 4, although we have failed to separate the B and C components from the radio core, let alone to resolve it into its two sub-components. The emission from the radio core is clearly stronger and more extended in IF2 which, in addition to the continuum, contains the CO-emission from the broad component (Figure 4b). A similar picture is seen for the narrow component in Figure 4c and d. Here, the radio core and B-component are separated in both IFs. The (large) negative spectral index ($\alpha \sim -1.7$) of the radio core rules out the possibility that the excess emission seen in the IF2-maps is due to an increase in continuum emission, since the IF2 maps are at a higher frequency than the IF1 maps. The B and C radio hot spots have even larger negative spectral indices (Carilli et al. 1997) and

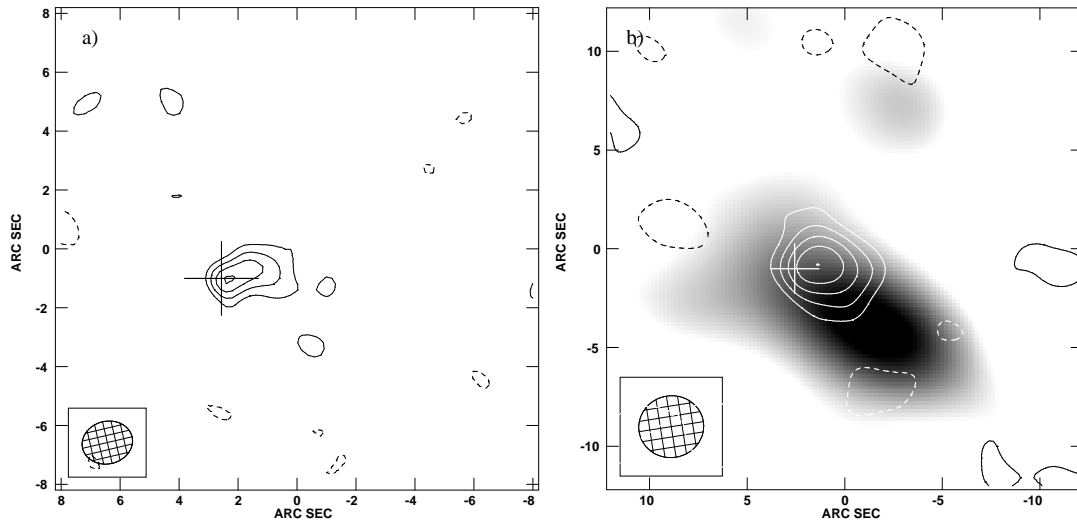


Fig. 5. **a)** Naturally weighted CO $J = 1 - 0$ map of the broad component obtained by combining the entire data-set and tapering it with a Gaussian with a half-width at 0.30 amplitude of $200\text{k}\lambda$. The spatial resolution is $1''.72 \times 1''.45$ with the major axis P.A.= 283° . The contours are at $-2, 2, 3, 4,$ and $5 \times \sigma$, where $\sigma = 35 \mu\text{Jy beam}^{-1}$. **b)** The CO $J = 1 - 0$ emission tapered down to $60\text{k}\lambda$ ($FWHM = 3''.33 \times 3''.12$) overlaid as contours on a gray-scale representation of the $J = 4 - 3$ emission by Papadopoulos et al. (2000). The contours are $-2, 2, 3, 4, 5,$ and 6σ with $\sigma = 0.4 \text{ mJy beam}^{-1}$, and the gray-scale range is $0.6 - 2.0 \text{ mJy beam}^{-1}$.

can therefore not be the cause of the increased emission either. This suggests that what we are seeing in the IF2 maps is continuum emission *plus* CO $J = 1 - 0$ emission from the emission features detected in the CO $J = 4 - 3$ maps.

4.1. The Broad Line Component

In order to disentangle the broad CO emission from the continuum, a box was put around the entire system and a CLEAN-component model of the continuum emission shown in Figure 4a was constructed. The CLEANing was stopped when the rms of the residuals reached the noise level in the image. This was then subtracted in uv-space from the IF2 data using the *AIPS* task UVSUB, resulting in uv-data from which maps free of continuum emission could be produced. Figure 5a shows the resulting CO $J = 1 - 0$ map of the broad component. The lack of residual emission at the positions of the two radio lobes demonstrates the effectiveness of the continuum emission subtraction. The CO $J = 1 - 0$ emission is detected at 5σ , peaking at a position which is coincident with the radio core position but with emission appearing to extend $2 - 3''$ to the west. In comparison, the broad component of the CO $J = 4 - 3$ emission was found to peak $\sim 4''$ south-west of the radio core (Papadopoulos et al. 2000).

In Figure 5b we have overlaid the CO $J = 1 - 0$ contours on top of a gray-scale image of the $J = 4 - 3$ emission. The $1 - 0$ map has been tapered down to $60\text{k}\lambda$ in order to better match the resolution of the $4 - 3$ data ($FWHM = 8''.9 \times 5''.5$). The offset between the centroids of the $1 - 0$ and $4 - 3$ emission is within the positional errors given the large $J = 4 - 3$ synthesized beam, and in

general there is good spatial correspondence between the two.

Assuming that the IF covers the entire line, we can estimate the velocity-integrated $J = 1 - 0$ flux density using

$$\int_{\Delta v} S_{\nu_{obs}} dv = \Delta\nu_{IF} \frac{c}{\nu_{obs}} S_{CO}, \quad (1)$$

where $\Delta\nu_{IF}$ is the width of the IF and S_{CO} is the flux density. We find $S_{CO} = (0.27 \pm 0.05) \text{ mJy}$ which yields a velocity-integrated flux density of $(0.15 \pm 0.03) \text{ Jy km s}^{-1}$, where we have used $\nu_{obs} = 24.035 \text{ GHz}$ and an IF bandwidth of 45 MHz (560 km s^{-1}) instead of 50 MHz due to bandpass rollover. The CO $J = 1 - 0$ emission from the broad component in the uvtaper 200 map appears to be somewhat extended in the north-west direction, although the low signal-to-noise of the data does not warrant a firm conclusion on this issue.

4.2. The Narrow Line Component

The continuum subtraction in the case of the narrow-line emission was done in a similar fashion as for the broad component: a continuum model was constructed by combining all IF1 channels and then subtracted from the IF2 channels. Since channels 1 and 2 had a different uv-coverage than channels 3 to 7 which again had a different uv-coverage than channels 8 and 9, three different continuum models had to be constructed, one for each of these three sets of channels. In order to increase the signal-to-noise ratio we averaged neighbouring channels during the imaging of the continuum-subtracted IF2 channels. We then searched for any residual emission at the expected position of the narrow component and used

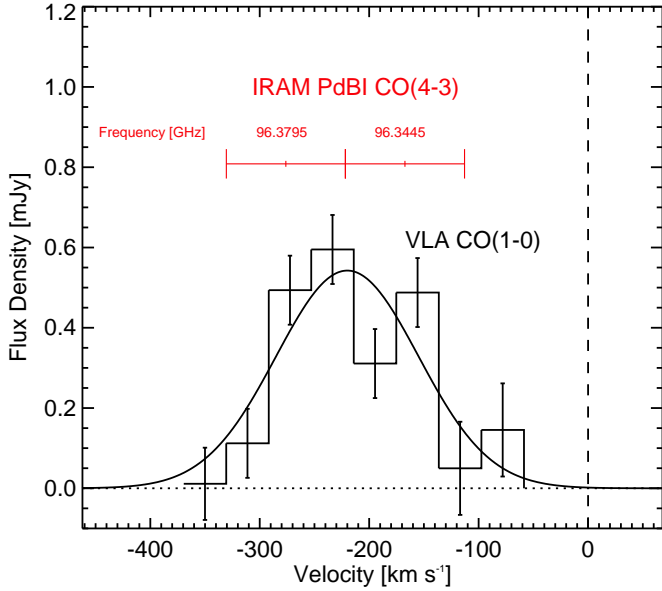


Fig. 6. The spectrum of the narrow CO $J = 1 - 0$ component in 4C 60.07. All channels maps were tapered with a $200\text{k}\lambda$ Gaussian. The rms noise in channels 1-2 is $0.12\text{ mJy beam}^{-1}$ at a spatial resolution of $1''.4 \times 1''.3$; the noise in channels 3-6 is $0.086\text{ mJy beam}^{-1}$ at a spatial resolution of $1''.7 \times 1''.4$, and the noise in channels 7-8 is $0.09\text{ mJy beam}^{-1}$ at a spatial resolution of $1''.9 \times 1''.5$. Above the line-profile we have plotted the velocity coverage of the channels in which $J = 4 - 3$ emission was detected (Papadopoulos et al. 2000). The vertical dashed line corresponds to the systemic velocity ($z = 3.788$).

the task IMEAN to measure the flux. The resulting spectrum of the CO $J = 1 - 0$ emission is shown in Figure 6 where we have also plotted the velocity-coverage of the two IRAM PdBI channels in which $J = 4 - 3$ emission from the narrow component was detected. Note that channels 1-2 and 8-9 are somewhat more noisy than the other channels, since the corresponding integration time is less. We detect CO $J = 1 - 0$ emission in channels 3 to 6, which in velocity-space overlaps with the two IRAM PdBI channels in which the strongest CO $J = 4 - 3$ emission is detected. Only very weak CO $J = 4 - 3$ emission was found in the third IRAM PdBI channel at 96.3095 GHz which is in agreement with the $J = 1 - 0$ line profile. From a Gaussian fit to the line profile, we find the $1 - 0$ spectrum to peak at $V \simeq (-220 \pm 40)\text{ km s}^{-1}$ offset from the systemic velocity of 4C 60.07 which is consistent with that found for the $4 - 3$ line given the large velocity bins. The formal linewidth is $\Delta V_{FWHM} \simeq (165 \pm 24)\text{ km s}^{-1}$, again in good agreement with that of the CO $J = 4 - 3$ line profile. The fit yields a velocity-integrated flux density of $0.09 \pm 0.01\text{ Jy km s}^{-1}$, see also Table 2.

Combining channels 3 to 6 we obtain the velocity-integrated CO $J = 1 - 0$ emission map shown in Figure 7a. In Figure 7b we have overlaid contours of the

CO $J = 1 - 0$ emission on a gray-scale image of the $J = 4 - 3$ emission where the latter has been tapered down to $60\text{ k}\lambda$. The $J = 1 - 0$ emission peaks at $\sim 0''.7$ east of the radio core which is consistent with the position of the narrow $J = 4 - 3$ component. Similar to what was found for the $J = 4 - 3$ line, in $J = 1 - 0$ the narrow component appears to be more compact and less extended than the broad component.

5. Discussion

5.1. CO Luminosity and Molecular Gas Mass

The observed CO $J = 1 - 0$ line fluxes for the broad and narrow components in 4C 60.07 imply intrinsic CO luminosities of $L'_{\text{CO}}(1 - 0) = (1.0 \pm 0.2) \times 10^{11}\text{ K km s}^{-1}\text{ pc}^2$ and $(6.0 \pm 0.7) \times 10^{10}\text{ K km s}^{-1}\text{ pc}^2$, respectively. For the $4 - 3$ line Papadopoulos et al. (2000) found $L'_{\text{CO}}(4 - 3) = (7 \pm 1) \times 10^{10}\text{ K km s}^{-1}\text{ pc}^2$ and $L'_{\text{CO}}(4 - 3) = (3.5 \pm 0.8) \times 10^{10}\text{ K km s}^{-1}\text{ pc}^2$ for the broad and narrow component, respectively, where we have computed the luminosities in the cosmology adopted here. From the CO $J = 1 - 0$ line the molecular gas mass can be found using the well-known relation $M(\text{H}_2) = X_{\text{CO}} L'_{\text{CO}}(1 - 0)$ which relates the CO $J = 1 - 0$ luminosity with the molecular gas mass (e.g. Strong et al. 1988). X_{CO} is the CO $J = 1 - 0$ line luminosity to H_2 -mass conversion factor which in the extreme UV-intense environments found in local Ultra Luminous Infra-Red Galaxies, and presumably also in high redshift galaxies such as 4C 60.07, has a value of about $0.8(\text{K km s}^{-1}\text{ pc}^2)^{-1}M_{\odot}$ (Downes & Solomon 1998). In doing so we find molecular gas masses of $M(\text{H}_2) \sim 8 \times 10^{10} M_{\odot}$ and $M(\text{H}_2) \sim 5 \times 10^{10} M_{\odot}$ for the broad and narrow CO emitting components, respectively. Hence, even for a conservative, non-Galactic value of X_{CO} we find that about $\sim 10^{11} M_{\odot}$ of molecular gas is associated with 4C 60.07. The estimated gas masses are in very good agreement with those of Papadopoulos et al. (2000).

The total gas mass in 4C 60.07 will of course be larger once the neutral hydrogen has been accounted for. Assuming a value of $M(\text{HI})/M(\text{H}_2) = 2$ which is typically found in IRAS galaxies (Andreani, Casoli, & Gerin 1995) we find a total gas mass of $M_{\text{gas}} = M(\text{H}_2) + 2M(\text{H}_2) = 2.4 \times 10^{11} M_{\odot}$ for the broad component and $1.5 \times 10^{11} M_{\odot}$ for the narrow component. In case that metal-poor gas is also present the gas mass can be even higher.

5.2. FIR Luminosity and star-formation efficiency

In the case where the far-IR luminosity is powered by a starburst and not an AGN, and all the stellar radiation is absorbed by dust, the far-IR to CO luminosity ratio, $L_{\text{FIR}}/L_{\text{CO}}$, provides a rough measure of the integrated luminosity of massive stars responsible for heating the dust (L_{FIR}) relative to the amount of fuel available for star formation (L'_{CO}). We estimate the far-IR luminosity of 4C 60.07 to be $L_{\text{FIR}} \simeq 4 \times 10^{13} L_{\odot}$, where

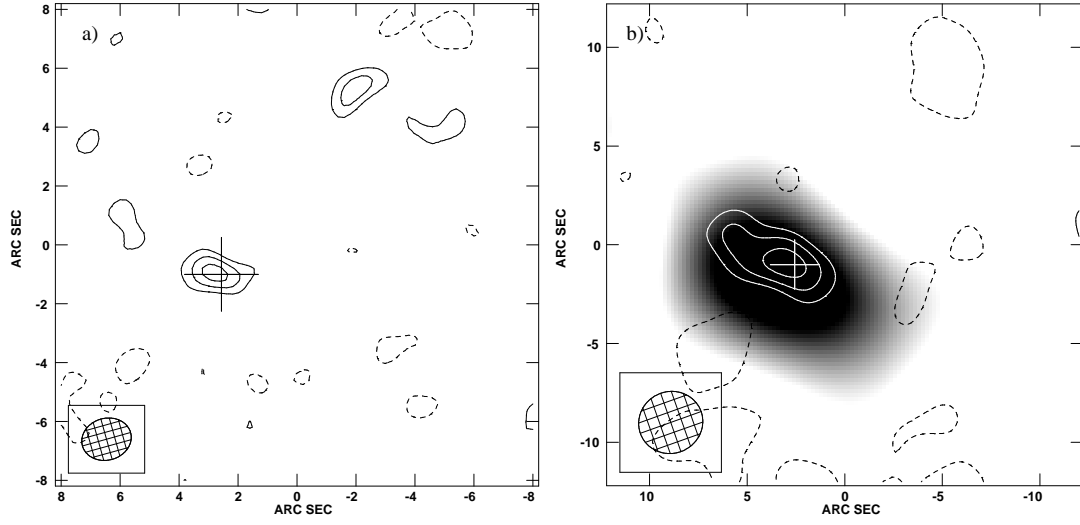


Fig. 7. **a)** The narrow component tapered at $200k\lambda$. The resolution is $1''.72 \times 1''.42$ at P.A. = 285° . Contours are at -2, 2, 3, and $4 \times \sigma$, where $\sigma = 55 \mu\text{Jy beam}^{-1}$. **b)** The CO $J = 1 - 0$ emission tapered down to $60k\lambda$ ($FWHM = 3''.22 \times 3''.07$) overlaid as contours on a gray-scale representation of the $J = 4 - 3$ detection by Papadopoulos et al. (2000). The contours are -2, 2, 3, and 4σ with $\sigma = 0.6 \text{ mJy beam}^{-1}$, and the gray-scale range is $0.6 - 2.0 \text{ mJy beam}^{-1}$.

Table 2. Observed and Derived Properties for 4C 60.07.

Parameter	4C 60.07 (broad)	4C 60.07 (narrow)
R.A.(J2000)	$05^h 12^m 54^s.75$	$05^h 12^m 55^s.30$
Decl.(J2000)	$+60^\circ 30' 50''.92$	$+60^\circ 30' 52''.29$
$S_{\text{CO}(1-0)}$ [mJy]	(0.27 ± 0.05)	(0.30 ± 0.10)
$S_{\text{CO}(1-0)} \Delta V$ [Jy km s^{-1}]	(0.15 ± 0.03)	(0.09 ± 0.01)
$L'_{\text{CO}(1-0)}$ [$\text{K km s}^{-1} \text{ pc}^2$]	$(1.0 \pm 0.2) \times 10^{11}$	$(6.0 \pm 0.7) \times 10^{10}$
$M(\text{H}_2)$ [M_\odot]	8×10^{10}	5×10^{10}

we have used the $850\text{-}\mu\text{m}$ flux measurement of Archibald et al. (2001) and adopted a dust temperature and spectral index of $T_d = 50 \text{ K}$ and $\beta = 1.5$, respectively. This yields a $L_{\text{FIR}}/L_{\text{CO}}$ ratio of $\simeq (4 \times 10^{13} L_\odot) / (1.6 \times 10^{11} \text{ K km s}^{-1} \text{ pc}^2) = 250 L_\odot (\text{K km s}^{-1} \text{ pc}^2)^{-1}$, which is similar to values found in ULIRGs (e.g. Solomon et al. 1997). Carilli et al. (2002a) found continuum-to-line ratios of 350 and 323 in the QSOs BRI 1202-0725 ($z = 4.70$) and BRI 1335-0417 ($z = 4.41$), respectively. A somewhat lower value of 200 was found in the $z = 4.12$ QSO PSS J2322+1944 (Carilli et al. 2002b).

The current star-formation rate measured in $M_\odot \text{ yr}^{-1}$ is given by

$$SFR \simeq (L_{\text{FIR}} 10^{-10} / L_\odot) \delta_{\text{MF}} \delta_{\text{SB}}, \quad (2)$$

where $\delta_{\text{MF}} \sim 0.8 - 2$ depends on the mass function of the stellar population, and δ_{SB} is the fraction of the far-IR luminosity which is powered by the starburst and not the AGN (Omont et al. 2001). If we adopt $\delta_{\text{MF}} = 0.8$ and conservatively assume that only 50% of L_{FIR} is powered by the starburst ($\delta_{\text{SB}} = 0.5$) we find $SFR \sim 1600 M_\odot \text{ yr}^{-1}$.

Assuming that the total amount of molecular gas observed towards 4C 60.07 ends up as fuel for the starburst, we find that there is enough molecular gas to sustain the inferred star-formation rate for $\sim 8 \times 10^7 \text{ yr}$. While this is short compared to the Hubble time it is still sufficient to produce a giant elliptical with a stellar mass of $M_* \simeq 10^{11} M_\odot$.

The efficiency with which stars are being formed, i.e. the rate of star-formation per solar mass of molecular hydrogen, is given by $SFE = SFR/M(\text{H}_2)$ or equivalently $L_{\text{FIR}}/M(\text{H}_2)$. For 4C 60.07 we find $SFE = L_{\text{FIR}}/M(\text{H}_2) \simeq 300 L_\odot M_\odot^{-1}$, which is somewhat higher than the $\sim 190 L_\odot M_\odot^{-1}$ reported by Papadopoulos et al. (2000) who derived their value based on their flux density measurement of $S_{850\mu\text{m}} = 11 \text{ mJy}$. Here we have used the measurement by Archibald et al. (2001) which yields a somewhat higher $850 \mu\text{m}$ flux density of 17 mJy , although still lower than the 22 mJy reported by Stevens et al. (2003).

Local ULIRGs exhibit star-formation efficiencies comparable to that of 4C 60.07, once the same X_{CO} -factor has been used (Solomon et al. 1997). It is worth stressing that our detection of CO $J = 1 - 0$ enables us to make a direct comparison of SFEs with that of local ULIRGs since the same gas mass measure (the $J = 1 - 0$ line) is used for ULIRGs.

The apparently high star-formation efficiencies found for the above systems, could be severely overestimated if the AGN contributes significantly to the far-IR luminosity. However, the detection of CO together with the fact that 4C 60.07 and other HzRGs appear extended on several tens of kilo-pc scales at submm-wavelengths (Ivison et al. 2000; Stevens et al. 2003) strongly suggests that the far-IR emission is powered by large-scale starburst and not the AGN. Here we must mention that while CO $J = 1 - 0$ may be a good indicator of the total metal-rich H_2 gas

reservoir, it may be a poor one regarding the dense gas phase ($n \geq 10^5 \text{ cm}^{-3}$) that "fuels" star-formation. The latter could be particular true in the tidally disrupted giant molecular clouds (GMCs) expected in ULIRGs where a diffuse phase may dominate the CO $J = 1 - 0$ emission but has little to do with star formation. This could be the reason why the L_{FIR}/L'_{CO} ratio is found to be such a strong function of L_{FIR} , increasing for the merger systems associated usually with large far-IR luminosities. Interestingly, recent work shows that the SFE of dense gas, parametrised by the $L_{FIR}/L_{HCN(1-0)}$ ratio (the HCN $J = 1 - 0$ critical density is $2 \times 10^5 \text{ cm}^{-3}$), remains constant from GMCs all the way to ULIRG system (Gao & Solomon 2003).

5.3. Excitation Conditions

From the detections of CO in 4C 60.07 we can infer the CO $(4-3)/(1-0)$ velocity/area-averaged brightness temperature ratio using $r_{43} = L'_{CO(4-3)}/L'_{CO(1-0)}$. The global line ratio, i.e. the line ratio obtained by combining the flux from the two components, is $r_{43} = 0.7^{+0.3}_{-0.2}$. The line ratios for the broad and narrow components are $0.7^{+0.3}_{-0.2}$ and $0.6^{+0.2}_{-0.2}$, respectively. Hence, given the large uncertainties we find no significant difference in the excitation conditions between the two components. Thus in this case H_2 mass estimates solely from CO $J = 4 - 3$ assuming full thermalisation and optical thickness of the latter (i.e. $r_{43} \simeq 1$) would not result in too large errors. However, the sub-thermal excitation of such high-J CO lines remains a possibility even in starburst environments (e.g. Papadopoulos & Ivison 2002; Greve et al. 2003).

In Figure 8 we plotted the velocity-integrated CO line flux densities (normalised to $J = 4 - 3$) for the broad and narrow components in 4C 60.07 as well as the normalised line fluxes for PSS J2322+1944. We have used a standard single-component large velocity gradient (LVG) code to interpret the observed line ratio. In fact, given the large range compatible with our measurements we can only put a lower limit on the density. Indeed, for both components the upper values for r_{43} are compatible with LTE and optically thick emission where the ratio is no longer sensitive to the density.

A lower limit on the average gas density can be set by the lowest possible value of $r_{43} = 0.4$ allowed by the observations. Adopting a typical CO abundance $\Lambda = X_{CO}/(dV/dr) = 10^{-5} (\text{km s}^{-1} \text{ pc}^{-1})^{-1}$, a $T_{CMB} = (1+z) \times 2.73 \text{ K} = 13.07 \text{ K}$ and a $T_{kin} = 50 \text{ K}$, which is a typical dust temperature in starburst environments (Colbert et al. 1999; Hughes et al. 1997), we find $n(\text{H}_2) \geq 2 \times 10^3 \text{ cm}^{-3}$. Adopting a higher $\Lambda = 10^{-4}$ (unlikely in such kinematically violent, UV-aggressive environments) lowers the aforementioned limit to $\sim 600 \text{ cm}^{-3}$. A lower assumed temperature of $T_{kin} = 30 \text{ K}$ does not change these lower limits by much. For the most likely value of $r_{43} = 0.7$ we find $n(\text{H}_2) = 3 \times 10^3 \text{ cm}^{-3}$ ($T_k = 50 \text{ K}$, $\Lambda = 10^{-5} (\text{km s}^{-1} \text{ pc}^{-1})^{-1}$).

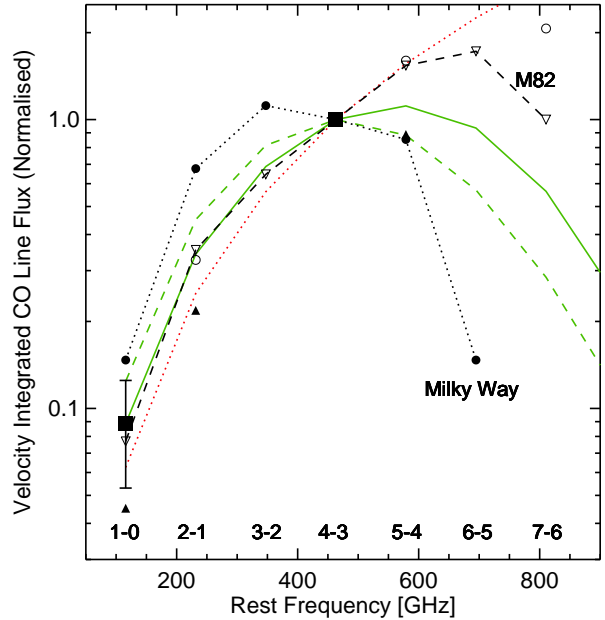


Fig. 8. Velocity-integrated CO line flux densities from 4C 60.07 are shown as filled squares. The integrated line fluxes have been normalised to the $J = 4 - 3$ line. Also shown are the line fluxes from the $z = 4.12$ QSO PSS J2322+1944 (filled triangles - Carilli et al. 2002b; Cox et al. 2002), the $z = 4.69$ QSO BRI 1202-0725 (open circles - Omont et al. 1996; Carilli et al. 2002a), the local starburst galaxy M82 (open triangles - Mao et al. 2000), and the integrated emission from within the solar radius of the the Milky Way (filled circles - Fixsen et al. 1999). The red dotted line shows the line flux increasing as frequency squared which is expected for optically thick conditions. The green lines show results from a LVG-model with $T_{kin} = 50 \text{ K}$, $X_{CO}/(dV/dr) = 10^{-5} (\text{km s}^{-1} \text{ pc}^{-1})^{-1}$, and $n(\text{H}_2)$ equal to $3.0 \times 10^3 \text{ cm}^{-3}$ (solid line) and $2.2 \times 10^3 \text{ cm}^{-3}$ (dashed line).

Comparing with the $z = 4.12$ QSO PSS J2322+1944 which has a $(4-3)/(1-0)$ line ratio of 1.4 ± 0.6 (Carilli et al. 2002b; Cox et al. 2002) it appears that the excitation conditions in 4C 60.07 are less extreme. Hence, these results may indicate that the molecular gas in 4C 60.07 is not as dense as that seen in PSS J2322+1944. Such a comparison, however, is prone to the effects of strong lensing. While 4C 60.07 is unlikely to be a strongly lensed system because of its CO components with widely different line widths, it is not the case for PSS 2322+1944 which is known to be lensed (Carilli et al. 2003). If the distribution of the $1 - 0$ and $J = 4 - 3$ emitting gas in the source plane differs, differential magnification of the two lines can result in erroneous intrinsic line ratios.

5.4. What is the Evolutionary Status of 4C 60.07?

A comparison between the molecular gas mass and the dynamical mass allows for the determination of the evolutionary status of a galaxy, while a comparison of its dynamical mass with that of present-day spiral or elliptical can point toward its possible descendant. Typically, dynamical masses are calculated assuming the gas is distributed in a disk in Keplerian rotation (e.g. Carilli et al. 2002a). In the case of 4C 60.07, however, we have sufficient spatial and kinematical information to conclude that the two gas components do not belong to such a structure. The detection of two kinematically distinct gas reservoirs in 4C 60.07, each with a large gas mass, suggest a major merger event. Hence, a more plausible scenario might be that the two clouds are part of spherical system in the process of collapsing. Assuming the system is virialised, one can apply the virial theorem to derive the following expression for the dynamical mass

$$M_{dyn} = 2.33 \times 10^9 \left(\frac{R}{\text{kpc}} \right) \left(\frac{\Delta V_{FWHM}}{100 \text{ km s}^{-1}} \right)^2 \left(\frac{1}{\alpha(1+q)} \right), \quad (3)$$

where q is a factor which described the influence of non-gravitational forces on the virial equilibrium, and α ranges from 0.55 to 2.4 with a typical value of 1.5 which we shall adopt here (see Bryant & Scoville (1996) for details). A possible caveat to this argument comes from the fact that if the assumption of a virialised system is not true, eq. 3 will tend to overestimate the true dynamical mass. Adopting a radius of the sphere corresponding to half the separation between the two components, i.e. $R \sim 15$ kpc (corresponding to $2''$), and a FWHM width equal to the velocity offset between the line centers of the two gas reservoirs, i.e. $\Delta V_{FWHM} \sim 700 \text{ km s}^{-1}$, leads to an enclosed dynamical mass of $M_{dyn} \lesssim 1.1 \times 10^{12} M_{\odot}$, where we have assumed that non-gravitational forces are negligible, i.e. $q \ll 1$. Note that since Bryant & Scoville (1996) derived eq. 3 by examining a large number of clouds filling up a spherical region, we have in the above assumed that the velocity and spatial separation between the two CO components is a fair approximation for ΔV_{FWHM} and R in eq. 3. Alternatively, we can do the more simple calculation of finding the virial mass required to keep the two clouds bound by a spherical potential. In this case the velocity dispersion becomes $\Delta V = (1/2)700 \text{ km s}^{-1} = 350 \text{ km s}^{-1}$, and we find $M_{virial} = G^{-1}R\Delta V^2 \simeq 4.3 \times 10^{11} M_{\odot}$, where we have assumed $R = 15$ kpc. Projection effects will only tend to make R and ΔV_{FWHM} , and therefore also the above mass estimates, larger. Thus, 4C 60.07 is a massive system with a dynamical mass comparable to that of giant elliptical galaxies seen in the present day Universe. The inferred ratio of the molecular-to-dynamic mass for the system as a whole is $M(\text{H}_2)/M_{dyn} \sim 0.12$, and the total gas fraction is $M_{gas}/M_{dyn} \sim 0.35$. The high gas fraction, along with the large velocity dispersion of the system suggest that 4C 60.07 is a very young system in its early stages of formation.

The fact that such a massive ($M_{dyn} \sim 10^{12} M_{\odot}$) system has assembled at $z = 3.8$, which corresponds to a time when the Universe was only $\sim 10\%$ of its present age, seems to favour the monolithic collapse model (e.g. Eggen, Lynden-Bell & Sandage 1962; Tinsley & Gunn 1976) of massive ellipticals over the hierarchical formation scenario (e.g. Baron & White 1987; Baugh et al. 1996; Kauffmann & Charlot 1998). Further in support of the monolithic collapse scenario is the large star-formation rate ($SFR \sim 1600 M_{\odot} \text{ yr}^{-1}$) we infer from the far-IR luminosity. If such a large star-formation rate can be sustained it is capable of producing a giant elliptical in a time scale comparable to the dynamical time. The dynamical time-scale for a system with a mass M within a radius R is

$$t_{dyn} = 7.42 \times 10^{11} \left(\frac{R}{\text{kpc}} \right)^{3/2} \left(\frac{M}{M_{\odot}} \right)^{-1/2}, \quad (4)$$

where t_{dyn} is measured in years (see p. 37 of Binney & Tremaine 1987). For a giant elliptical with a mass $M_{ell} = 10^{12} M_{\odot}$ and a radius $R = 30$ kpc, we find $t_{dyn} \simeq 1.2 \times 10^8 \text{ yr}$. Hence, in order to form a giant elliptical within a dynamical time scale, star-formation rates of the order $M_{ell}/t_{dyn} \simeq 8000 M_{\odot} \text{ yr}^{-1}$ are required, which is comparable to what we find in 4C 60.07. It is important to note that even if the true dynamical mass or the star-formation rate of this system are less than the above estimates, the fact that at $z = 3.8$ about $1.3 \times 10^{11} M_{\odot}$ in H_2 gas mass alone has assembled within 15 kpc points towards a major galaxy forming merger rather than a gradual accumulation of mass over time and redshift. This mass can only be revised upwards and typically reach $\sim 4 \times 10^{11} M_{\odot}$ if HI is also accounted for, thereby making the case for a monolithic collapse scenario even stronger.

4C 60.07 is not the only system with extended CO emission. Molecular gas distributed on tens of kpc scales, sometimes in separate gas components, have been observed in high redshifts quasars (e.g. Carilli et al. 2002a; Papadopoulos et al. 2001) and radio galaxies (De Breuck et al. 2003; De Breuck et al. in prep.). Thus, there is evidence to show that at least some luminous active galaxies in the early Universe, in addition to harbouring super-massive black holes in their centres, are associated with massive reservoirs of molecular gas distributed on tens of kpc scales which are in the process of merging. This observed coequality between large scale mergers of gaseous subsystems and the epoch of AGN-activity might provide clues to the origin of the tight relationship observed locally between the velocity dispersion of spheroids and the mass of their central black holes (Ferrarese & Merritt 2000).

Acknowledgements. TRG acknowledges support from the Danish Research Council and from the EU RTN Network POE. PPP acknowledges a Marie Curie Individual Fellowship HPMT-CT-2000-00875. We are grateful to Ignas Snellen and Philip Best for useful advice on *AZPS*. We are also greatly indebted to Carlos De Breuck and Michiel Reuland for providing us with the IRAM PdBI CO $J = 4 - 3$ data.

References

- Andreani, P., Casoli, F., & Gerin, M. 1995, *A&A*, 300, 43.
- Archibald, E.N., Dunlop, J.S., Hughes, D.H., Rawlings, S., Eales, S. & Ivison, R.J. 2001, *MNRAS*, 323, 417.
- Baron, E. & White, S.D.M. 1987, *ApJ*, 322, 585.
- Baugh, C.M., Cole, S. & Frenk, C.S. 1996, *MNRAS*, 283, 136.
- Binney, J. & Tremaine, S. 1987, "Galactic Dynamics", Princeton Series on Astrophysics, Princeton University Press.
- Bryant, P.M. & Scoville, N.Z. 1996, *ApJ*, 457, 678.
- Carilli, C.L., Röttgering, H.J.A., van Ojik, R., Miley, G.K. & van Breugel, W.J.M. 1997, *ApJS*, 109, 1.
- Carilli, C.L., Kohno, K., Kawabe, R., Ohta, K., Henkel, C., Menten, K.M., Yun, M.S., Petric, A. & Tutui, Y. 2002a, *AJ*, 123, 1838.
- Carilli, C.L., Cox, P., Bertoldi, F., Menten, K.M., Omont, A., Djorgovski, S.G., Petric, A., Beelen, A., Isaak, K.G. & McMahon, R.G. 2002b, *ApJ*, 575, 145.
- Carilli, C.L., Lewis, G.F., Djorgovski, S.G., Mahabal, A., Cox, P., Bertoldi, F., & Omont, A. 2003, *Science*, 300, 773.
- Chambers, K.C., Miley, G.K., van Breugel, W.J.M., Bremer, M.A.R., Huang, J.-S. & Trentham, N.A. 1996, *ApJS*, 106, 247.
- Colbert, J.W., Malkan, M.A., Clegg, P.E., Cox, P., Fischer, J., Lord, S.D., Luhman, M., Satyapal, S., Smith, H.A., Spinoglio, L., Stacey, G., & Unger, S.J. 1999, *ApJ*, 511, 721.
- Cox, P., Omont, A., Djorgovski, S.G., Bertoldi, F., Pety, J., Carilli, C.L., Isaak, K.G., Beelen, A., McMahon, R.G. & Castro, S. 2002, *A&A*, 387, 406.
- De Breuck, C., Neri, R., Morganti, R., Omont, A., Rocca-Volmerange, B., Stern, D., Reuland, M., van Breugel, M., Röttgering, H.J.A., Stanford, S.A., Spinrad, H., Vigotti & M., Wright, M. 2003a, *A&A*, 401, 911.
- De Breuck, Neri, R. & Omont, A. 2003b, "Radio Galaxies: Past, present and future", Leiden, 11-15 Nov 2002, eds. M. Jarvis et al.
- Downes, D., Solomon, P.M. & Radford, S.J.E. 1993, *ApJ*, 414, L13.
- Downes, D. & Solomon, P.M. 1998, *ApJ*, 506, 615.
- Dunlop, J.S., Hughes, D.H., Rawlings, S., Eales, S. & Ward, M. 1994, *Nature*, 370, 347.
- Eggen, O.J., Lynden-Bell, D. & Sandage, A.R. 1962, *ApJ*, 136, 748.
- Fanaroff, B.L. & Riley, J.M. 1974, *MNRAS*, 167, 31.
- Ferrarese, L. & Meritt, D. 2000, *ApJ*, 539, L9.
- Fixsen, D.J., Bennett, C.L., & Mather, J.C. 1999, *ApJ*, 526, 207.
- Gao, Y. & Solomon, P.M. 2003, in "Star formation at high angular resolution", IAU Symposium No 221, Sydney Australia, p.95.
- Greve, T.R., Ivison, R.J., & Papadopoulos, P.P. 2003, *ApJ*, in press.
- Guilloteau, S., Omont, A., Cox, P., McMahon, R. & Petitjean, P. 1999, *A&A*, 349, 363.
- Hughes, D.H., Dunlop, J.S. & Rawlings, S. 1997, *MNRAS*, 289, 766.
- Ivison, R.J., Dunlop, J.S., Hughes, D.H., Archibald, E.N., Stevens, J.A., Holland, W.S., Robson, E.I., Eales, S.A., Rawlings, S., Dey, A., & Gear, W. K. 1998, *ApJ*, 494, 211.
- Ivison, R.J., Dunlop, J.S., Smail, I., Dey, A., Liu, M.C., & Graham, J.R. 2000, *ApJ*, 542, 27.
- Kauffmann, G. 1996, *MNRAS*, 281, 487.
- Kauffmann, G. & Charlot, S. 1998, *MNRAS*, 294, 705.
- Mao, R.Q., Henkel, C., Schulz, A., Zielinsky, M., Mauersberger, R., Störzer, H., Wilson, T.L., & Gensheimer, P. 2000, *A&A*, 358, 433.
- McLure, R.J. & Dunlop, J.S. 2000, *MNRAS*, 317, 249.
- Omont, A., Petitjean, P., Guilloteau, S., McMahon, R.G., Solomon, P.M., & Pecontal, E. 1996, *Nature*, 382, 428.
- Omont, A., Cox, P., Bertoldi, F., McMahon, R.G., Carilli, C., & Isaak, K.G., 2001, *A&A*, 374, 371.
- Papadopoulos, P. P., Röttgering, H. J. A., van der Werf, P. P., Guilloteau, S., Omont, A., van Breugel, W. J. M. & Tilanus, R. P. J. 2000, *ApJ*, 528, 626.
- Papadopoulos, P.P. & Ivison, R.J. 2002, *ApJ*, 564, L9.
- Papadopoulos, P.P., Ivison, R.J., Carilli, C.L., & Lewis, G. 2001, *Nature*, 409, 58.
- Röttgering, H., van Ojik, R., Miley, G., Chambers, K., van Breugel, W. & de Koff, S. 1997 *A&A*, 326, 505.
- Solomon, P.M., Downes, D., Radford, S.J.E. & Barrett, J.W. 1997, *ApJ*, 478, 144.
- Stevens, J.A., Ivison, R.J., Dunlop, J.S., Smail, I., Percival, W.J., Hughes, D.H., Röttgering, H.J.A., van Breugel, W.J.M. & Reuland, M. 2003, *Nature*, 425, 264.
- Strong, A. W., Bloemen, J. B. G. M., Dame, T. M., Grenier, I. A., Hermsen, W., Lebrun, F., Nyman, L.-A., Pollock, A. M. T. & Thaddeus, P. 1988, *A&A*, 201, 1.
- Tinsley, B.M. & Gunn, J.E. 1976, *ApJ*, 203, 52.
- West, M.J. 1994, *MNRAS*, 268, 79.